Radiolabeled polyoxometalate clusters: Kidney dysfunction evaluation and tumor diagnosis by positron emission tomography imaging

Dalong Ni [a], Dawei Jiang [a, b], Hyung-Jun Im [a, c], Hector F. Valdovinos [a, e], Bo Yu [a], Shreya Goel [d], Todd E. Barnhart [a, e], Peng Huang [a, b], Weibo Cai [a, d, e, f, *]

[a] Department of Radiology, University of Wisconsin-Madison, Wisconsin, USA
[b] Guangdong Key Laboratory for Biomedical Measurements and Ultrasound Imaging, School of Biomedical Engineering, Shenzhen University, Shenzhen, China
[c] Department of Transdisciplinary Studies, Graduate School of Convergence Science and Technology, Seoul National University, Seoul, South Korea
[d] Materials Science Program, University of Wisconsin-Madison, Wisconsin, USA
[e] Department of Medical Physics, University of Wisconsin-Madison, Wisconsin, USA
[f] University of Wisconsin Carbone Cancer Center, Wisconsin, USA

ARTICLE INFO

ABSTRACT

Radiolabeled nanoprobes for positron emission tomography (PET) imaging has received special attention over the past decade, allowing for sensitive, non-invasive, and quantitative detection of different diseases. The rapidly renal clearable nanomaterials normally suffer from a low accumulation in the tumor through the enhanced permeability and retention (EPR) effect due to the rapidly reduced concentration in the blood circulation after renal clearance. It is highly important to design radiolabeled nanomaterials which can meet the balance between the rapid renal clearance and strong EPR effect within a suitable timescale. Herein, renal clearable polyoxometalate (POM) clusters of ultra-small size (~1 nm in diameter) were readily radiolabeled with the oxophilic ^{89}Zr to obtain ^{89}Zr-POM clusters, which may allow for efficient staging of kidney dysfunction in a murine model of unilateral ureteral obstruction (UUO). Furthermore, the as-synthesized clusters can accumulate in the tumor through EPR effect and self-assemble into larger nanostructures in the acidic tumor microenvironment for enhanced tumor accumulation, offering an excellent balance between renal clearance and EPR effect.

© 2018 Elsevier Ltd. All rights reserved.

1. Introduction

Positron emission tomography (PET) imaging is routinely used tools in the clinic for noninvasive imaging due to its high sensitivity, unlimited tissue penetration, and quantitative detection [1–5]. Consequently, considerable attention has been paid to the development of radiolabeled nanoprobes for whole body imaging, *in vivo* pharmacokinetic studies, and nanooncology applications [6–8]. Throughout the past decade, various radiolabeled nanomaterials, including gold nanoparticles (NPs, labeled with ^{68}Ga/^{64}Cu) [9–13], silica NPs (labeled with ^{18}F/^{64}Cu/^{89}Zr) [14–18], iron oxide NPs (labeled with ^{64}Cu/^{72}As/^{69}Ge) [19–25], ^{18}F-labeled upconversion NPs [26–28], ^{64}Cu-labeled organic NPs [29,30], transition metal sulfides [31–33], and nanographene [34], have shown great potential for *in vivo* PET imaging. However, most of these radiolabeled nanoprobes face major challenges for clinical translation because of difficulties in large-scale synthesis, poor targeting performance to specific diseases (such as cancer), and high accumulation in reticuloendothelial system (RES) organs (e.g., liver and spleen). For example, a considerable portion of NPs was captured by the liver as discovered by PET imaging after intravenous injection of ^{89}Zr-silica or ^{64}Cu-porphysomes NPs [16,29]. The accumulation of ^{64}CuAuNPs in the spleen was even higher than 200 %ID/g at 24 h postinjection (p.i.) [10]. In addition, these radiolabeled nanoprobes were mainly cleared out through the hepatobiliary route over a long time (more than a month in some cases), which greatly hindered their potential for clinical translation.

For most clinical imaging agents, renal clearance is desirable which can avoid toxicity caused by extended retention time *in vivo*. Since the pioneering work on renal clearable quantum dots [35], fabrication of radiolabeled nanoprobes with renal clearance

provides an alternative for not only cancer diagnosis but also kidney disease assessment with PET imaging. Almost 10% of all adults are subjected to a variety of kidney diseases, which is difficult to detect with the current diagnostic techniques at an early stage but could cause kidney failure later on [36]. Renal clearable radio-labeled nanomaterials may allow for noninvasive staging of kidney dysfunction, which is highly desirable to deepen our fundamental understanding of the kidney disease progression [37]. However, the rapidly renal clearable nanomaterials normally suffer from a low accumulation and a short retention time in the target sites (such as the tumor) [38]. Thus, it is very beneficial to design radiolabeled nanoprobes which can balance the imaging requirement and renal clearance within a suitable timescale.

Herein, renal clearable Mo-based polyoxometalate (POM) clusters were synthesized by an easy, large-scale, and low-cost method, which were ionic compounds that consisted of cations (Na^+ and NH^{4+}) and macroanionic units ($PMo_{12}O_{40}^{n-}$) [39]. An oxophilic radioisotope, ^{89}Zr ($t_{1/2}$: 3.3 days), was conveniently labeled to the oxygen-rich POM cluster to obtain ^{89}Zr-POM without additional chelators such as desferrioxamine (DFO) [15]. The extended blood circulation of ^{89}Zr-POM clusters (a distribution half-life of 9.86 min and a blood elimination half-life of 9.57 h) is highly beneficial for *in vivo* PET imaging, improving passive accumulation and prolonging retention time at the target sites. The ^{89}Zr-POM clusters, mainly excreted through the renal system, can be successfully applied for noninvasive staging of kidney dysfunction *via* dynamic PET imaging, which was confirmed on a well-established preclinical murine model of unilateral ureteral obstruction (UUO). Moreover, the as-synthesized clusters can accumulate in the tumor through enhanced permeability and retention (EPR) effect and self-assemble into larger nanostructures in the acidic tumor microenvironment for enhanced tumor accumulation and extended retention. The long circulation time, as well as the pH-driven self-assembly strategy, endows these radiolabeled clusters with an excellent EPR effect, obtaining the optimal balance of renal clearance and EPR effect or imaging applications.

2. Experimental section

Hexaammonium molybdate tetrahydrate (($NH_4)_6Mo_7O_{24} \cdot 4H_2O$), sodium dihydrogen phosphate (NaH_2PO_4), and L-ascorbic acid were purchased from Sigma-Aldrich. All reagents were of analytical grade and used without any purification.

2.1. Synthesis of POM clusters

A facile one-pot approach as we reported previously was used to synthesize the POM clusters [39]. First, 2 mmol of ($NH_4)_6Mo_7O_{24} \cdot 4H_2O$ was dissolved in ultrapure water (10 mL) with continuous stirring at 25 °C. A 5 mL solution of 1.17 mmol of NaH_2PO_4 was then rapidly added. Subsequently, another 2 mL solution of saturated L-ascorbic acid (in ultrapure water) was added dropwise into the system under stirring. After further stirring for 15 min, the resulting POM clusters were precipitated by adding 80 mL of ethanol, collected by centrifugation, washed with water and ethanol three times, and finally dispersed in water or phosphate-buffered saline (PBS) for further use.

2.2. ^{89}Zr-labeling and serum stability studies

Briefly, for ^{89}Zr-labeling, 100 μL of POM clusters dispersed in 4-(2-hydroxyethyl)-1-piperazineethanesulfonic acid (HEPES) buffer was directly mixed with 1 mCi (or 37 MBq) of ^{89}Zr-oxalate at 37 °C. The final pH value of the mixture was adjusted to 7–8 with 1 M Na_2CO_3. After shaking for 2 h, ^{89}Zr-POM was precipitated from the

solvent by adding ethanol and collected by centrifugation and finally dispersed in PBS for *in vivo* application. ^{89}Zr labeling yield was monitored and quantified by using thin layer chromatography (TLC), which acquired at 37 °C using PBS (pH = 5) as the developing solvent. Free $^{89}Zr(IV)$ was used as a control. ^{89}Zr-POM will move front with the developing solvent while the free $^{89}Zr(IV)$ will remain at the origin at such low pH without chelating with ethylenediaminetetraacetic acid (EDTA).

For stability studies, ^{89}Zr-POM was incubated in PBS with different pH value (pH = 5, 6.5, and 7.4) at 37 °C for up to 24 h (the time period investigated for PET imaging). The mixture were sampled at different time points and precipitated from the solvent by adding 1 mL of ethanol. The centrifugate was collected, and the radioactivity was measured by a gamma counter (PerkinElmer). The percentages of intact ^{89}Zr on the ^{89}Zr-POM clusters were calculated using the equation (radioactivity of centrifugates/total radioactivity × 100%.).

To further confirmed the stability, the stability of, ^{89}Zr-POM was incubated in PBS with different pH value (pH = 5, 6.5, and 7.4) for 48 h was also measured by the thin layer chromatography (TLC), which acquired at 37 °C using PBS (pH = 5) as the developing solvent. Free $^{89}Zr(IV)$ was used as a control.

2.3. UUO model

The murine model of unilateral ureteral obstruction (UUO), a well-established preclinical model for kidney dysfunction, was established according to the literature [40]. UUO mice were achieved by complete ligation of the left ureter near the renal pelvis while the right ureter was kept intact. UUO mice at 2 days post-obstruction were used as the early stage while the UUO mice at 21 days post-obstruction were applied to the end stage.

In vivo dynamic PET imaging: For dynamic scanning of healthy mice, a group of healthy mice (n = 4) was injected with 150 μL (~115 μCi or 4.255 MBq) of ^{89}Zr-POM in PBS. A 30 min dynamic scan was performed by using a microPET/CT Inveon small animal scanner (Siemens Medical Solutions USA, Inc.). Image reconstruction and ROI analysis of the PET data were conducted using vendor software (Inveon Research Workplace [IRW]) on decay-corrected whole-body images.

For dynamic scanning of UUO mice, a group of UUO mice was injected with 150 μL (~70 μCi or 2.59 MBq) of ^{89}Zr-POM in PBS. A 30 min dynamic scan was performed by using a microPET/CT Inveon small animal scanner (Siemens Medical Solutions USA, Inc.). The dynamic quantitative uptake of the left kidney (UUO) and right kidney (normal) within 30 min was used to evaluate kidney function through ROI analysis using vendor software (Inveon Research Workplace [IRW]) on decay-corrected whole-body images.

In vivo PET imaging of 4T1 tumor-bearing mice: 4T1 tumor-bearing BALB/c mice were established and used for *in vivo* PET imaging: 4T1 cells (10^6 in 100 μL PBS) were subcutaneously injected into the right front flank of BALB/c mice to establish the 4T1 tumor model. Hematoxylin-eosin (H&E) staining was performed after treatments to validate the establishment of the model.

The tumor-bearing mice were anesthetized, and 150 μL (~140 μCi or 5.18 MBq) of ^{89}Zr-POM in PBS was intravenously injected into 4T1 tumor-bearing mice (n = 3). PET scans at various time point postinjection were performed by using a microPET/CT Inveon small animal scanner (Siemens Medical Solutions USA, Inc.). ROI analysis of each PET scan was performed to calculate the percentage of injected dose per gram of tissue (%ID/g) values in mouse organs and tumor, using vendor software (Inveon Research Workplace [IRW]) on decay-corrected whole-body images.

Biodistribution analysis was carried out to confirm the quantitative uptake obtained through PET imaging. After the last *in vivo*

PET imaging at 24 h p.i., all major tissues and organs were collected and wet-weighed. The radioactivity in each tissue and organ was measured using a gamma counter and calculated as %ID/g.

2.4. In vivo photothermal imaging of POM clusters

The photothermal properties of the clusters were firstly evaluated. The POM (100 ppm Mo) was illuminated by an 808 nm laser for 5 min (0.8 and 1.5 W/cm^2) and the pure water solution was used as a control. The temperature change was monitored by an FLIR™ E50 camera.

For *in vivo* photothermal imaging, the tumor-bearing mice were exposed to 808 nm laser with an output power density of 1.5 W/cm^2 for 5 min at 6 h after intravenous injection of POM (35 mg Mo/kg). Tumor temperature and thermal images were visualized and recorded using the FLIR™ E50 camera.

2.5. Cell culture and cytotoxicity assessment

Murine breast cancer 4T1 cells was cultured at 37 °C and with 5% CO_2 in Roswell Park Memorial Institute medium (RPMI) 1640 supplemented with 10% fetal bovine serum (FBS) and 1% penicillin/streptomycin. Human embryonic kidney 293 (HEK293) cells were cultured at 37 °C with 5% CO_2 in Dulbecco's Modified Eagle Medium (DMEM) supplemented with 10% fetal bovine serum (FBS) and 1% penicillin/streptomycin. Cells were seeded into a 96-well cell culture plate at 10^6/well and then incubated for 24 h at 37 °C under 5% CO_2. Culture media solutions of POM with different concentrations (0, 50, 100, 250, and 500 μg of Mo per mL) were added to the wells. The cells were then incubated for 24 h at 37 °C under 5% CO_2, and the cell viability was measured by MTT assay.

2.6. Histological assessment

The *in vivo* biocompatibility of POM clusters was evaluated using standard H&E staining. BALB/c mice were euthanized at 1 day and 30 days post intravenous injection of POM (70 mg Mo/kg in saline). Tissues were H&E-stained to monitor the histological changes in the heart, liver, spleen, lung and kidney of mice. The histological sections were observed under an inverted optical microscope (Nikon, Eclipse Ti-U, Japan).

2.7. Statistical analysis

Statistical comparisons were performed by using a Student's two-tailed *t*-test. Quantitative data were expressed as mean ± s.d, *: $P < 0.05$; **: $P < 0.01$; ***: $P < 0.001$.

2.8. Characterization

Transmission electron microscopy images were acquired on an FEI T12 microscope with an accelerating voltage of 120 kV. UV–vis spectra were recorded on Agilent Cary 60 spectrophotometer. Dynamic light scattering (DLS) measurements were conducted on Nano-Zetesizer (Malvern Instruments Ltd). The elemental concentrations (i.e. Mo) were measured with inductively coupled plasma optical emission spectrometry (ICP-OES). Photothermal imaging was recorded on an FLIR™ E50 camera.

3. Results and discussion

3.1. Synthesis and characterization of ^{89}Zr-POM clusters

The blue and highly hydrophilic POMs, synthesized *via* an easy, fast, and large-scale process at a low cost [39], were highly stable in various media (Figs. S1-S2). As shown in transmission electron microscopy (TEM) image (Fig. 1a), these clusters were uniform with an average diameter of ~1 nm at pH 7.4 and could self-assemble into larger nanostructures with a diameter of ~25 nm at pH 6.5, where the collapsed nano-vesicles during the sample preparation process were observed in the TEM image (Fig. 1b). These nanostructures further aggregated into larger ones through additional acidification to pH 5.0 (Fig. 1c). Dynamic light scattering (DLS) measurement confirmed such increase in size after acidification, from 2.5 ± 0.3 nm in a neural medium to 401 ± 22 nm after acidification (Fig. 1d, Fig. S3). The pH-responsive self-assembly of POM clusters was also monitored by UV–vis–NIR spectra, where the pH-driven self-assembly of POM resulted in a significant blue-shift of the main peak towards 808 nm and an enhanced absorption (Fig. S4). The reduced electrostatic repulsions and increased attractive forces, resulting from the hydrogen bond formation of POM macroanions through acid-induced protonation, was likely responsible for such low-pH-driven self-assembly [39,41,42]. As the extracellular tumor milieu (pH = 6.5–6.8) and endocytic organelles (pH = 5.0–6.0) both exhibit a low pH value [43–45], such low-pH-driven self-assembly of POM clusters is highly beneficial for cancer diagnosis and treatment [46].

Among the medically relevant isotopes, ^{89}Zr is highly oxophilic and can be readily labeled to the oxygen-rich matrix [15]. In this work, we used the oxygen-rich POM cluster to bind ^{89}Zr without additional chelators. By mixing ^{89}Zr-oxalate and POM clusters at 37 °C with constant shaking, ^{89}Zr was immediately bound to POM clusters to form ^{89}Zr-POM with a high labeling yield of ~80% in 10 min, as detected by thin layer chromatography (TLC). An acidic solution (pH = 5) was used as developing solvent, where free ^{89}Zr would stay at the original spot and ^{89}Zr-POM would move up to the solvent front (inset in Fig. 1f). After shaking for 2 h, the labeling yield was ~95% (Fig. 1e). Moreover, ^{89}Zr-POM clusters were highly stable in phosphate-buffered saline (PBS) with various pH values for 24 h and 48 h (Figs. S5-6). As shown by X-ray diffraction (XRD) pattern (Fig. 1f), the framework of the synthesized POM nanoclusters after radiolabeling remained the same. Moreover, both DLS and UV–vis–NIR spectra results showed that the aggregation behavior of POM was not affected after the ^{89}Zr labeling (Figs. S7-8), which was reasonably expected since the amount of 89Zr used for radiolabeling was extremely little (<1 nmol/mCi). A standard MTT assay showed a negligible toxicity of POM clusters to both human embryonic kidney 293 (HEK293) cells and murine breast cancer 4T1 cells (Fig. S9).

3.2. In vivo dynamic PET imaging of normal mice

Encouraged by the highly efficient and stable chelator-free labeling of ^{89}Zr-POM, *in vivo* dynamic PET imaging (30 min) of ^{89}Zr-POM in healthy mice was performed (n = 4) with a microPET/CT Inveon small animal scanner. As showed in the maximum intensity projection (MIP) images (Fig. 2a), the blood pool showed a stable signal of ^{89}Zr-POM throughout the dynamic imaging process. The time-activity curve of ^{89}Zr-POM in the blood (Fig. 2b) showed that these clusters were rapidly distributed into the body with a short distribution half-life ($t_{1/2\alpha}$) of 9.86 ± 3.11 min and circulated in the body with a long-time blood elimination half-life ($t_{1/2\beta}$) of 9.57 ± 3.04 h, indicating an excellent *in vivo* circulation of ^{89}Zr-POM. The half-life of other kinds of POMs depends on their hydrated size, *in vivo* stability, and protein binding ability [47]. Herein, our proposed radiolabeling method can be expanded to radiolabel other kinds of POMs with ^{89}Zr for the investigation of their *in vivo* pharmacokinetics using PET as a powerful tool. Moreover, in light of the excellent sensitivity and quantification ability of dynamic PET imaging, the half-life calculated based on *in vivo* dynamic PET is
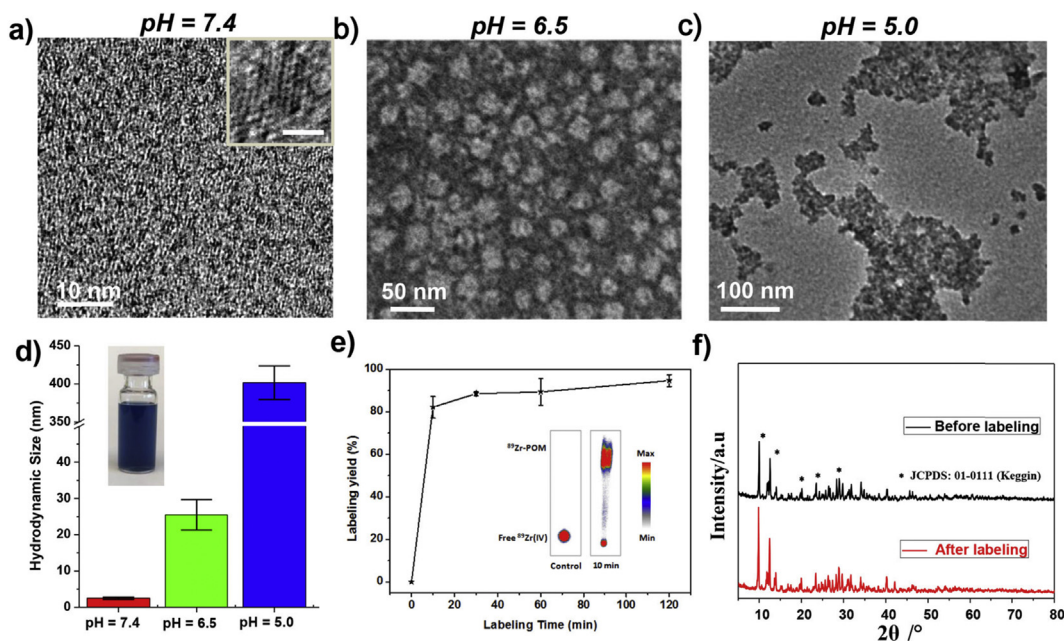
Fig. 1. Synthesis and characterization of [89]Zr-POM clusters. a - c) TEM images of POM clusters at pH = 7.4, 6.5, and 5.0. Insert in a) shows the High-resolution TEM image of one POM, scale bar: 1 nm. d) DLS measurements of POM clusters with successive acidifications from pH = 7.4 to pH = 6.5 and to pH = 5.0 (inset: photograph of the clusters dispersed in water). e) Time-dependent [89]Zr-labeling yield in HEPES buffer solution with POM clusters. Inset: the autoradiographic image of TLC plates of [89]Zr-POM clusters acquired at 37 °C using PBS (pH = 5) as the developing solvent. Free [89]Zr(IV) was used as a control. f) Powder X-ray diffraction (XRD) of POM nanoclusters before and after radiolabeling with [89]Zr.

much more accurate than our previously reported values based on the measurement of Mo concentration in blood with inductively coupled plasma optical emission spectrometry (ICP-OES) [39]. The signal from the kidneys can be found at 1 min p.i., and it took about ~225 s for kidneys to reach their maximal uptake values (27.9 ± 14.3 %ID/g, Fig. S8). Kidney and bladder became the dominant uptake organs after 5 min p.i., indicating predominant renal clearance of [89]Zr-POM. The bladder uptake continued to increase during the whole dynamic scan period, with 29.9 ± 22.1 %ID/g of bladder observed at the end of dynamic PET imaging (Fig. S10-11). The renal filtration and urinary excretion of [89]Zr-POM clusters was attributed to their ultrasmall hydrodynamic diameter of 2.5 nm in a neutral medium (Fig. S3). The clearance and biodistribution of POM clusters have been investigated in our previous work, where more than 91% injected dose (ID) was excreted in one week [39].

### 3.3. In vivo dynamic PET imaging of UUO mice

Ureteropelvic junction obstruction is typically asymptomatic at an early stage but can lead to renal failure if not treated timely in newborns [48]. Unilateral ureteral obstruction (UUO) murine model, a common model to evaluate the ureteropelvic junction obstruction, was built by completely ligating the left ureter of the mouse while the right ureter was kept intact (Fig. 3a). Real-time monitoring of kidney clearance kinetics of [89]Zr-POM clusters by *in vivo* dynamic PET imaging to noninvasively stage the kidney dysfunction will facilitate our understanding of kidney diseases (Figs. 3—4). As shown in Fig. 3b—c, the UUO left kidney (UUO LK) can be easily differentiated from the unobstructed right kidneys in an early stage, where only the crescent-shaped kidney cortex was found in UUO LK resulting from the blocked outflow upon obstruction (Fig. 4). The peak uptake value of UUO LK was found to be 20.1 ± 7.5 %ID/g, which was much less than that of the contra-lateral right kidney (RK, 80.9 ± 21.8%ID/g). The signal of LK remained almost unchanged after the peak while the signal in RK decreased sharply, indicating a dramatically reduced blood

perfusion to the LK upon the obstruction. The peak value of RK in UUO mice was much higher than that in normal mice (Fig. S10), which may be contributed to the less clearance of UUO LK [49]. For UUO mice at end stage (day 21 after the ureteral obstruction), the UUO LK completely failed as confirmed by the H&E staining, in which most of the glomerular and tubular structures were destroyed and replaced with inflammatory cells and/or fibrotic tissue (Fig. S12). No signal could be found in UUO end stage LK (Fig. 3e—f) throughout the dynamic scanning, while the RK exhibited normal renal function.

At the end of the 30-min dynamic PET scanning, the signal of the UUO LK at an early stage (i.e. some uptake but no clearance) was much higher than that of the RK (i.e. rapid clearance), while an opposite trend was found for UUO at the end stage (LK: no uptake; RK: rapid clearance; Fig. 3d). The excretion of [89]Zr-POM clusters to renal pelvis was highly limited in early stage UUO LK, and most of them stayed in the renal cortex (Fig. 4). For end stage UUO LK, no [89]Zr-POM clusters was found in the UUO LK, and most clusters were cleared through the right kidney. The [89]Zr-POM clusters-based PET imaging offers a simple, minimally invasive, and quantitative test of renal function which does not require urine or blood samples. More importantly, this tracer may allow for quantification of split renal function based on the PET images while serum biomarker detection (e.g., Cr and BUN test) struggle to provide much detailed information of each kidney. Besides, several radiotracers such as ^{18}F-fluoride [50,51], ^{68}Ga-EDTA [52] and ^{99m}Tc-MAG3 [49] have also been reported to noninvasively evaluate renal function, which, however, suffers from the singal imaging function mode while [89]Zr-POM could also be applied for tumor diagnosis and therapy simultaneously [39,46].

3.4. In vivo PET imaging of 4T1-tumor bearing mice

A well-known phenomenon is that nanoparticles (NPs) often passively accumulate in tumor through the EPR effect, which has played pivotal roles in cancer diagnosis and therapy. Designing of
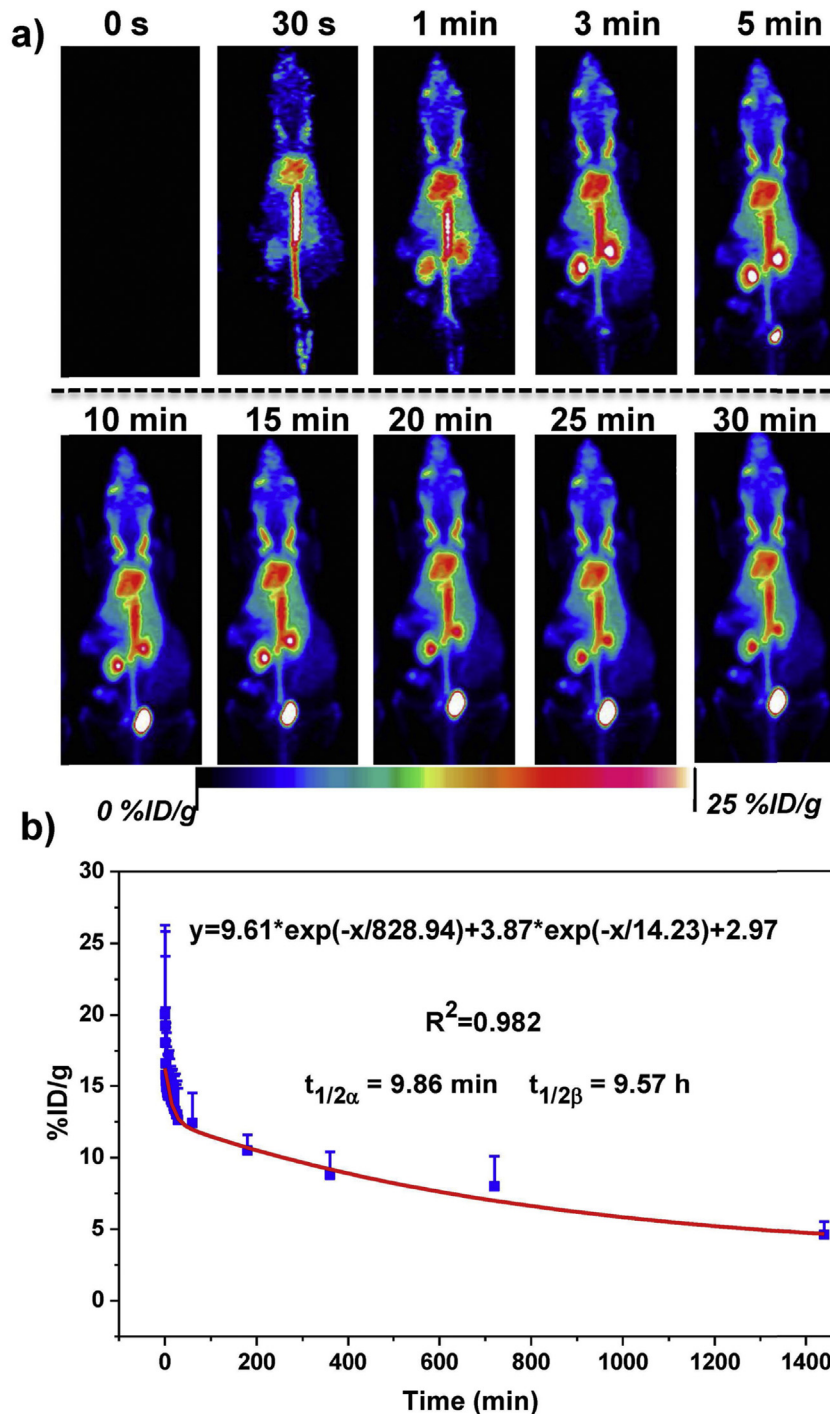
Fig. 2. a) Representative dynamic PET images of healthy mice after intravenous injection of [89]Zr-POM clusters within different time points. b) Time-activity curves of [89]Zr-POM in the blood (n = 4, mean ± s.d.).

renal clearable NPs with a strong EPR effect will render these NPs unique in cancer imaging. One of the major pitfalls of renal clearable NPs is their poor EPR effect because of the rapid clearance from the bloodstream or the backflow of NPs from the tumor site [38]. Ultra-small size and surface modification endowing NPs (such as Au NPs) with short distribution half-life and longer blood-elimination half-life are common strategies to balance between renal clearance and tumor accumulation [53–56]. As mentioned above, the [89]Zr-POM clusters displayed excellent blood circulation with a short distribution half-life ($t_{1/2\alpha}$) of 9.86 ± 3.11 min and a

long blood-elimination half-life ($t_{1/2\beta}$) of 9.57 ± 3.04 h. Such a long $t_{1/2\beta}$ exceeds the minimal requirement of 6 h for a strong EPR effect [57], and is over 4 times longer than that of cysteine-coated QDs (~2 h) [35], making these clusters more suitable for tumor imaging due to a much slower renal clearance than our previous reported ^{64}Cu-labeled GSH-Au NPs ($t_{1/2\alpha}$ = 0.73 min; $t_{1/2\beta}$ = 5.81 min) [58]. Moreover, the POM clusters could self-assemble into bigger nanostructures in response to tumor acidic microenvironment (Fig. 1a–e), which would hold back the outflow of NPs from tumor sites to enhance tumor accumulation and prolong the tumor
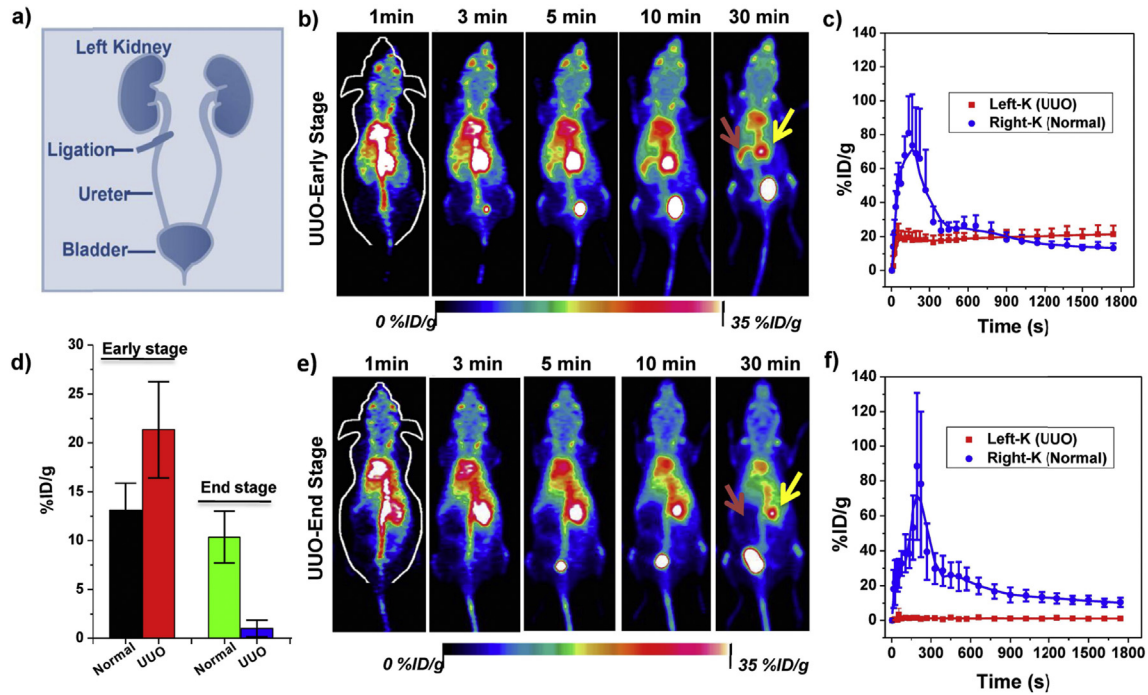
Fig. 3. PET imaging of unilateral ureteral obstruction (UUO) in mice with [89]Zr-POM clusters. a) A schematic illustration of the UUO model in mice. b) Representative dynamic PET maximum intensity projection (MIP) images within different time points and time−activity curves of UUO early stage mice (b, c) or end stage (e, f) after intravenous injection of [89]Zr-POM clusters. d) Comparison of kidney uptake at 30 min p.i. in UUO early and end stage mice. Red arrows point to the left kidney (UUO) and yellow arrows point to the right kidney (normal). (For interpretation of the references to colour in this figure legend, the reader is referred to the Web version of this article.)
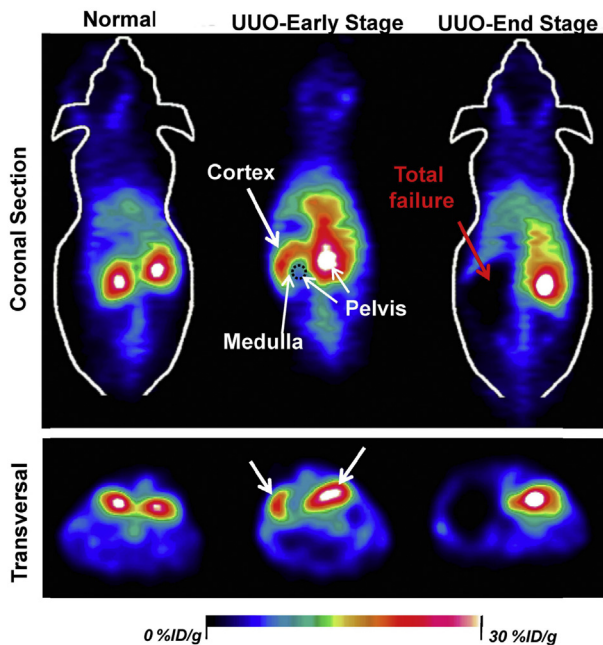
Fig. 4. Representative coronal and transversal PET imaging slices of staging kidneys between normal function, mild, and severe dysfunction within 10 min after intravenous injection of [89]Zr-POM clusters. The renal uptake of [89]Zr-POM clusters was remarkably reduced in UUO left kidney, while the changes were minimal in contralateral right kidney both in UUO early and end-stage.

retention time.

Based on above considerations, aside from the staging of kidney dysfunction, *in vivo* PET imaging of tumor was also carried out *via* intravenous injection of [89]Zr-POM clusters into 4T1-tumor bearing

mice (n = 3). Free [89]Zr radioisotope was injected into another group of 4T1-tumor-bearing mice as a control. Serial PET scans were performed to monitor the tumor uptake and renal clearance of the tracer. The coronal slices containing the tumor at different time points were shown in Fig. 5a−b. As expected, [89]Zr-POM clusters allowed for an efficient and time-dependent delineation of the tumor (Fig. 5a), as early as 3 h p.i. (6.0 ± 1.9 %ID/g) and the tumor uptake peaked at around 6 h p.i. (7.5 ± 1.4 %ID/g). The tumor remained visible at 24 h p.i., and the tumor uptake was determined to be 6.5 ± 1.2 %ID/g at 24 h p.i., which was even higher than our previously reported ^{64}Cu-labeled silica NPs conjugated with tumor-targeting TRC105 antibody (*e.g.*, peak value of 5.9 ± 0.4 %ID/g at ~5 h p.i.) [59]. Such a high tumor accumulation was believed to be due to the strong EPR effect resulting from the long blood-elimination half-life and self-assembly capability of [89]Zr-POM clusters in the acidic tumor microenvironment [41,42]. In contrast, the tumor could be hardly displayed with [89]Zr alone, and the tumor uptake of free [89]Zr was found to be significantly lower at all time points examined. High bone uptake was found in free [89]Zr-injected mice (Fig. 5b) which was consistent with previous results [16], while the [89]Zr-POM clusters exhibited very low bone uptake, indicating the excellent labeling stability of [89]Zr-POM clusters *in vivo*.

Radioactivity signal in the kidneys remained high at all examined time points (Fig. 5 c), further demonstrating that [89]Zr-POM clusters could clear from the blood to the kidneys, which was consistent with previous results of healthy and UUO mice. However, the liver accumulation increased over time (Fig. 5c), which may be caused by serum protein adsorption of clusters in biological fluid or adsorption of opsonins on [89]Zr-POM (known as "opsonization") *in vivo*, which initiates the recognition of macrophages in RES organs such as the liver and spleen [60,61]. These results were consistent with our previous results that nearly 18% ID of POM clusters were excreted through the liver metabolism, while 73% ID of the clusters were cleared through the renal system in one week
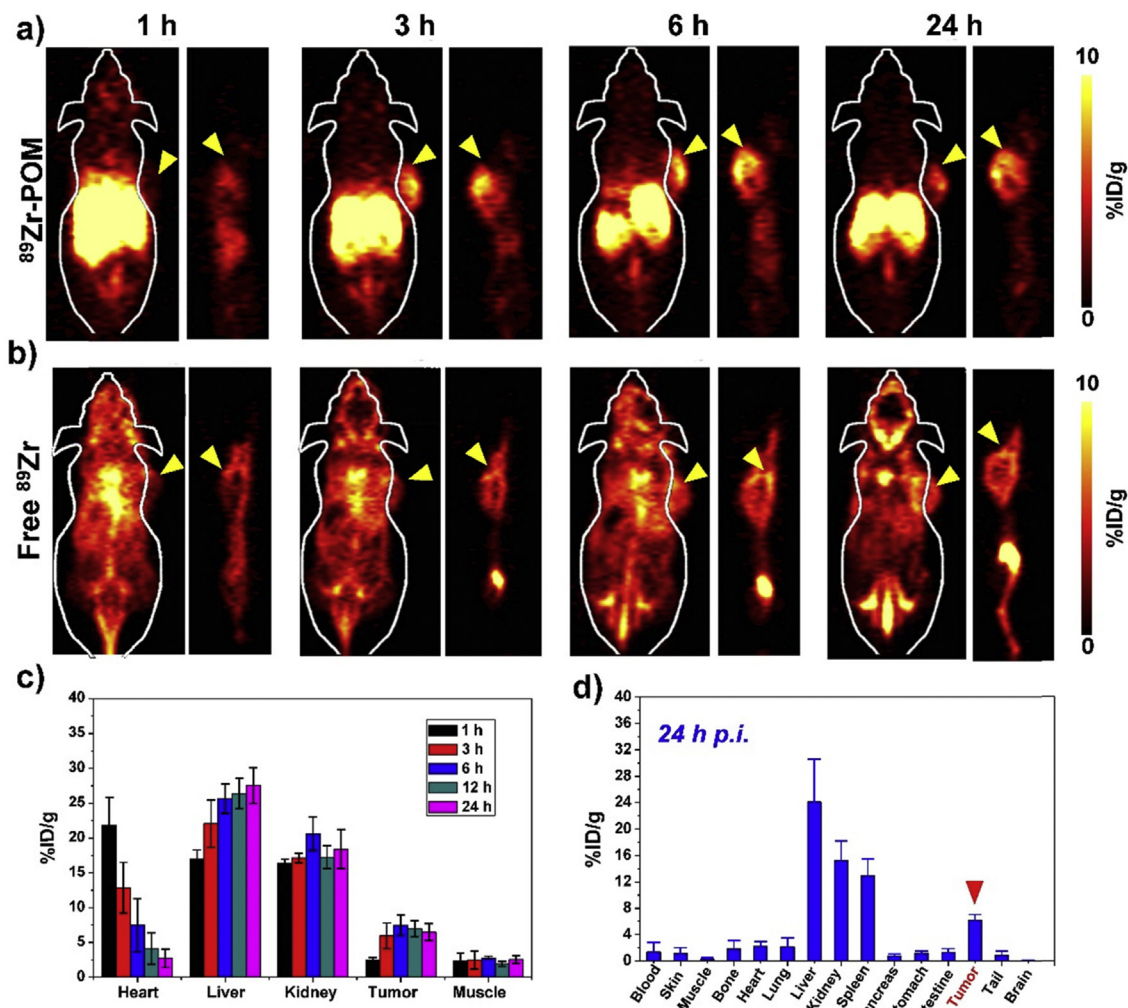
Fig. 5. Representative coronal and sagittal PET imaging slices of 4T1-tumor bearing mice (tumors indicated by arrowheads) after intravenous injection of a) ^{89}Zr-POM clusters and b) free^{89}Zr as control at different time points. c) Quantification of ^{89}Zr-POM uptake in the blood, liver, spleen, kidney, 4T1 tumor, and muscle at various time points post-injection (n = 3, mean ± s.d.). d) Biodistribution of ^{89}Zr- POM clusters at 24 h after intravenous injection into 4T1-tumor bearing mice as determined by ^{89}Zr radioactivity measurement in various tissues and organs (n = 3, mean ± s.d.).

[39].

To further validate the accuracy of PET quantification analysis, *ex vivo* biodistribution studies were performed at 24 h p.i. (after the last PET scan). As shown in Fig. 5d, the 4T1 tumor uptake at 24 h p.i. was 6.1 ± 0.9 %ID/g, which matched well with our PET data. The liver, spleen, and kidney had significant uptake at 24 h p.i. as these organs were responsible for clearance of ^{89}Zr-POM clusters. In addition, the extra L-ascorbic acid must be completely removed after the synthesis of POM clusters, ensuring that the ^{89}Zr was labeled with POM at pH of 7–8 to avoid unstable radiolabeled clusters (Fig. S13). It is worth noting that these POM clusters exhibit strong NIR absorption (Fig. S4), which could convert the NIR energy into heat for tumor photothermal therapy (Fig. S14). Photothermal imaging of 4T1 tumor-bearing mice after intravenous injection of ^{89}Zr-POM clusters at 24 h p.i. under 808 nm laser irradiation for 5 min showed an elevated temperature at the tumor site (~62.4 °C; Fig. S15), which further demonstrated the accumulation of POM clusters in the tumor area for tumor photothermal therapy. Lastly, H&E staining of various mouse organs (heart, liver, spleen, lung, and kidneys) after intravenous injection of POM clusters showed no noticeable organ damage or inflammatory lesions over one month (Fig. S16), suggesting the low *in vivo* toxicity of the POM clusters.

Taken together these finding, our PET studies in 4T1 tumor-bearing mice demonstrated the effective balance and synergy of renal clearance and EPR effect, using the long circulating and pH-responsive self-assembling ^{89}Zr-POM clusters.

4. Conclusion

In summary, we present here the renal clearable ^{89}Zr-POM clusters, synthesized by a large-scale, low-cost, and chelate-free labeling method, for noninvasive staging of both the kidney dysfunction and tumor progression. The ultra-small ^{89}Zr-POM clusters exhibited desirable blood circulation *in vivo* ($t_{1/2\alpha}$ = 9.86 ± 3.11 min; $t_{1/2\beta}$ = 9.57 ± 3.04 h.), which can act like "molecular nanoprobes" to bridge the conventional concepts of "small molecule probes" and "nanotechnology" in the PET area. Dynamic PET imaging of ^{89}Zr-POM clusters on UUO mice successfully differentiated the UUO kidney at both early and end stage. Moreover, the long blood-elimination half-life, as well as the pH-responsive self-assembly of ^{89}Zr-POM clusters in the acidic tumor tissue, endowed these clusters with both efficient renal clearance and excellent EPR effect in a murine model. Together, the findings in this work indicated broad potential of radiolabeled POM clusters

for various future applications in many diseases such as cancer and kidney dysfunction, which are currently under investigation in our laboratory.

Notes

The authors declare no competing financial interest.

Acknowledgements

Appendix A. Supplementary data

Supplementary data related to this article can be found at https://doi.org/10.1016/j.biomaterials.2018.04.019.

References

[1] T. Doerks, R.R. Copley, J. Schultz, C.P. Ponting, P. Bork, Systematic identification of novel protein domain families associated with nuclear functions, Genome Res. 12 (2002) 47–56.
[2] M.E. Phelps, Positron emission tomography provides molecular imaging of biological processes, Proc. Natl. Acad. Sci. U.S.A. 97 (2000) 9226–9233.
[3] K.C. Black, A. Ibricevic, S.P. Gunsten, J.A. Flores, T.P. Gustafson, J.E. Raymond, et al., In vivo fate tracking of degradable nanoparticles for lung gene transfer using PET and Cerenkov imaging, Biomaterials 98 (2016) 53–63.
[4] S.M. Ametamey, M. Honer, P.A. Schubiger, Molecular imaging with PET, Chem. Rev. 108 (2008) 1501–1516.
[5] T.M. Shaffer, E.C. Pratt, J. Grimm, Utilizing the power of Cerenkov light with nanotechnology, Nat. Nanotechnol. 12 (2017) 106–117.
[6] S. Goel, C.G. England, F. Chen, W. Cai, Positron emission tomography and nanotechnology: a dynamic duo for cancer theranostics, Adv. Drug Deliv. Rev. 113 (2017) 157–176.
[7] S. Goel, F. Chen, E.B. Ehlerding, W. Cai, Intrinsically radiolabeled nanoparticles: an emerging paradigm, Small 10 (2014) 3825–3830.
[8] Y. Xing, J. Zhao, P.S. Conti, K. Chen, Radiolabeled nanoparticles for multi-modality tumor imaging, Theranostics 4 (2014) 290–306.
[9] J. Frigell, I. Garcia, V. Gomez-Vallejo, J. Llop, S. Penades, 68Ga-labeled gold glyconanoparticles for exploring blood-brain barrier permeability: preparation, biodistribution studies, and improved brain uptake via neuropeptide conjugation, J. Am. Chem. Soc. 136 (2014) 449–457.
[10] Y. Zhao, D. Sultan, L. Detering, S. Cho, G. Sun, R. Pierce, et al., Copper-64-alloyed gold nanoparticles for cancer imaging: improved radiolabel stability and diagnostic accuracy, Angew. Chem. Int. Ed. 53 (2014) 156–159.
[11] A.F. Frellsen, A.E. Hansen, R.I. Jolck, P.J. Kempen, G.W. Severin, P.H. Rasmussen, et al., Mouse positron emission tomography study of the biodistribution of gold nanoparticles with different surface coatings using embedded Copper-64, ACS Nano 10 (2016) 9887–9898.
[12] X. Sun, X. Huang, X. Yan, Y. Wang, J. Guo, O. Jacobson, et al., Chelator-free (64)Cu-integrated gold nanomaterials for positron emission tomography imaging guided photothermal cancer therapy, ACS Nano 8 (2014) 8438–8446.
[13] H. Hu, P. Huang, O.J. Weiss, X. Yan, X. Yue, M.G. Zhang, et al., PET and NIR optical imaging using self-illuminating (64)Cu-doped chelator-free gold nanoclusters, Biomaterials 35 (2014) 9868–9876.
[14] T.M. Shaffer, S. Harmsen, E. Khwaja, M.F. Kircher, C.M. Drain, J. Grimm, Stable radiolabeling of sulfur-functionalized silica nanoparticles with Copper-64, Nano Lett. 16 (2016) 5601–5604.
[15] T.M. Shaffer, M.A. Wall, S. Harmsen, V.A. Longo, C.M. Drain, M.F. Kircher, et al., Silica nanoparticles as substrates for chelator-free labeling of oxophilic radioisotopes, Nano Lett. 15 (2015) 864–868.
[16] F. Chen, S. Goel, H.F. Valdovinos, H. Luo, R. Hernandez, T.E. Barnhart, et al., In vivo integrity and biological fate of chelator-free zirconium-89-labeled mesoporous silica nanoparticles, ACS Nano 9 (2015) 7950–7959.
[17] D. Ni, D. Jiang, E.B. Ehlerding, P. Huang, W. Cai, Radiolabeling silica-based nanoparticles via coordination chemistry: basic principles, strategies, and applications, Acc. Chem. Res. 51 (2018) 778–788.
[18] X. Huang, F. Zhang, S. Lee, M. Swierczewska, D.O. Kiesewetter, L. Lang, et al., Long-term multimodal imaging of tumor draining sentinel lymph nodes using mesoporous silica-based nanoprobes, Biomaterials 33 (2012) 4370–4378.
[19] R. Torres Martin de Rosales, R. Tavare, R.L. Paul, M. Jauregui-Osoro, A. Protti, A. Glaria, et al., Synthesis of 64Cu(II)-bis(dithiocarbamatebisphosphonate) and its conjugation with superparamagnetic iron oxide nanoparticles: in vivo evaluation as dual-modality PET-MRI agent, Angew. Chem. Int. Ed. 50 (2011) 5509–5513.
[20] R. Chakravarty, H.F. Valdovinos, F. Chen, C.M. Lewis, P.A. Ellison, H. Luo, et al., Intrinsically germanium-69-labeled iron oxide nanoparticles: synthesis and in-vivo dual-modality PET/MR imaging, Adv. Mater. 26 (2014) 5119–5123.
[21] F. Chen, P.A. Ellison, C.M. Lewis, H. Hong, Y. Zhang, S.X. Shi, et al., Chelator-free synthesis of a dual-modality PET/MRI agent, Angew. Chem. Int. Ed. 52 (2013) 13319–13323.
[22] X. Cui, S. Belo, D. Kruger, Y. Yan, R.T. de Rosales, M. Jauregui-Osoro, et al., Aluminium hydroxide stabilised MnFe2O4 and Fe3O4 nanoparticles as dual-modality contrasts agent for MRI and PET imaging, Biomaterials 35 (2014) 5840–5846.
[23] D. Patel, A. Kell, B. Simard, J. Deng, B. Xiang, H.Y. Lin, et al., Cu2+-labeled, SPION loaded porous silica nanoparticles for cell labeling and multifunctional imaging probes, Biomaterials 31 (2010) 2866–2873.
[24] X. Yang, H. Hong, J.J. Grailer, I.J. Rowland, A. Javadi, S.A. Hurley, et al., cRGD-functionalized, DOX-conjugated, and (6)(4)Cu-labeled superparamagnetic iron oxide nanoparticles for targeted anticancer drug delivery and PET/MR imaging, Biomaterials 32 (2011) 4151–4160.
[25] J. Xie, K. Chen, J. Huang, S. Lee, J. Wang, J. Gao, et al., PET/NIRF/MRI triple functional iron oxide nanoparticles, Biomaterials 31 (2010) 3016–3022.
[26] Q. Liu, Y. Sun, C.G. Li, J. Zhou, C.Y. Li, T.S. Yang, et al., 18F-labeled magnetic-upconversion nanophosphors via rare-earth cation-assistant ligand assembly, ACS Nano 5 (2011) 3146–3157.
[27] Y. Sun, M. Yu, S. Liang, Y. Zhang, C. Li, T. Mou, et al., Fluorine-18 labeled rare-earth nanoparticles for positron emission tomography (PET) imaging of sentinel lymph node, Biomaterials 32 (2011) 2999–3007.
[28] Q. Liu, M. Chen, Y. Sun, G. Chen, T. Yang, Y. Gao, et al., Multifunctional rare-earth self-assembled nanosystem for tri-modal upconversion luminescence/fluorescence/positron emission tomography imaging, Biomaterials 32 (2011) 8243–8253.
[29] T.W. Liu, T.D. MacDonald, J. Shi, B.C. Wilson, G. Zheng, Intrinsically copper-64-labeled organic nanoparticles as radiotracers, Angew. Chem. Int. Ed. 51 (2012) 13128–13131.
[30] Y. Zhang, M. Jeon, L.J. Rich, H. Hong, J. Geng, S. Shi, et al., Non-invasive multimodal functional imaging of the intestine with frozen micellar naph-thalocyanines, Nat. Nanotechnol. 9 (2014) 631–638.
[31] M. Zhou, R. Zhang, M. Huang, W. Lu, S. Song, M.P. Melancon, et al., A chelator-free multifunctional [64Cu]CuS nanoparticle platform for simultaneous micro-PET/CT imaging and photothermal ablation therapy, J. Am. Chem. Soc. 132 (2010) 15351–15358.
[32] X. Sun, X. Huang, J. Guo, W. Zhu, Y. Ding, G. Niu, et al., Self-illuminating 64Cu-doped CdSe/ZnS nanocrystals for in vivo tumor imaging, J. Am. Chem. Soc. 136 (2014) 1706–1709.
[33] A. Riedinger, T. Avellini, A. Curcio, M. Asti, Y. Xie, R. Tu, et al., Post-synthesis incorporation of (6)(4)Cu in CuS nanocrystals to radiolabel photothermal probes: a feasible approach for clinics, J. Am. Chem. Soc. 137 (2015) 15145–15151.
[34] S. Shi, C. Xu, K. Yang, S. Goel, H.F. Valdovinos, H. Luo, et al., Chelator-free radiolabeling of nanographene: breaking the stereotype of chelation, Angew. Chem. Int. Ed. 56 (2017) 2889–2892.
[35] H.S. Choi, W. Liu, P. Misra, E. Tanaka, J.P. Zimmer, B. Itty Ipe, et al., Renal clearance of quantum dots, Nat. Biotechnol. 25 (2007) 1165–1170.
[36] L.S. Chawla, P.W. Eggers, R.A. Star, P.L. Kimmel, Acute kidney injury and chronic kidney disease as interconnected syndromes, N. Engl. J. Med. 371 (2014) 58–66.
[37] N. Kamaly, J.C. He, D.A. Ausiello, O.C. Farokhzad, Nanomedicines for renal disease: current status and future applications, Nat. Rev. Nephrol. 12 (2016) 738–753.
[38] M. Yu, J. Zheng, Clearance pathways and tumor targeting of imaging nano-particles, ACS Nano 9 (2015) 6655–6674.
[39] C. Zhang, W. Bu, D. Ni, C. Zhang, Q. Li, et al., A polyoxometalate cluster paradigm with self-adaptive electronic structure for acidity/reducibility-specific photothermal conversion, J. Am. Chem. Soc. 138 (2016) 8156–8164.
[40] M. Yu, J. Zhou, B. Du, X. Ning, C. Authement, L. Gandee, et al., Noninvasive staging of kidney dysfunction enabled by renal-clearable luminescent gold nanoparticles, Angew. Chem. Int. Ed. 55 (2016) 2787–2791.
[41] T. Liu, M.L. Langston, D. Li, J.M. Pigga, C. Pichon, A.M. Todea, et al., Self-recognition among different polyprotic macroions during assembly processes in dilute solution, Science 331 (2011) 1590–1592.
[42] T. Liu, E. Diemann, H. Li, A.W. Dress, A. Muller, Self-assembly in aqueous solution of wheel-shaped Mo154 oxide clusters into vesicles, Nature 426 (2003) 59–62.
[43] Y. Wang, K. Zhou, G. Huang, C. Hensley, X. Huang, X. Ma, et al., A nanoparticle-based strategy for the imaging of a broad range of tumours by nonlinear amplification of microenvironment signals, Nat. Mater. 13 (2014) 204–212.
[44] I.F. Tannock, D. Rotin, Acid pH in tumors and its potential for therapeutic exploitation, Cancer Res. 49 (1989) 4373–4384.
[45] P. Mi, D. Kokuryo, H. Cabral, H. Wu, Y. Terada, T. Saga, et al., A pH-activatable nanoparticle with signal-amplification capabilities for non-invasive imaging of tumour malignancy, Nat. Nanotechnol. 11 (2016) 724–730.
[46] D. Ni, D. Jiang, H.F. Valdovinos, E.B. Ehlerding, B. Yu, T.E. Barnhart, et al., Bioresponsive polyoxometalate cluster for redox-activated photoacoustic imaging-guided photothermal cancer therapy, Nano Lett. 17 (2017) 3282–3289.
[47] J.T. Rhule, C.L. Hill, D.A. Judd, R.F. Schinazi, Polyoxometalates in medicine,

Chem. Rev. 98 (1998) 327—358.

[48] S. Decramer, S. Wittke, H. Mischak, P. Zurbig, M. Walden, F. Bouissou, et al., Predicting the clinical outcome of congenital unilateral ureteropelvic junction obstruction in newborn by urinary proteome analysis, Nat. Med. 12 (2006) 398—400.

[49] M.N. Tantawy, R. Jiang, F. Wang, K. Takahashi, T.E. Peterson, D. Zemel, et al., Assessment of renal function in mice with unilateral ureteral obstruction using 99mTc-MAG3 dynamic scintigraphy, BMC Nephrol. 13 (2012) 168.

[50] U. Schnockel, S. Reuter, L. Stegger, E. Schlatter, K.P. Schafers, S. Hermann, et al., Dynamic 18F-fluoride small animal PET to noninvasively assess renal function in rats, Eur. J. Nucl. Med. Mol. Imag. 35 (2008) 2267—2274.

[51] R. Werner, H. Wakabayashi, X. Chen, M. Hirano, T. Shinaji, C. Lapa, et al., Novel functional renal imaging with 18F-FDS PET in rat models of kidney diseases, J. Nucl. Med. (2017), https://doi.org/10.2967/jnumed.117.203828.

[52] M.S. Hofman, R.J. Hicks, Gallium-68 EDTA PET/CT for renal imaging, Semin. Nucl. Med. 46 (2016) 448—461.

[53] J. Liu, M. Yu, C. Zhou, S. Yang, X. Ning, J. Zheng, Passive tumor targeting of renal-clearable luminescent gold nanoparticles: long tumor retention and fast normal tissue clearance, J. Am. Chem. Soc. 135 (2013) 4978—4981.

[54] J. Liu, M. Yu, X. Ning, C. Zhou, S. Yang, J. Zheng, PEGylation and zwitterionization: pros and cons in the renal clearance and tumor targeting of near-IR-emitting gold nanoparticles, Angew. Chem. Int. Ed. 52 (2013) 12572—12576.

[55] D. Ni, Z. Shen, J. Zhang, C. Zhang, R. Wu, J. Liu, et al., Integrating anatomic and functional dual-mode magnetic resonance imaging: design and applicability of a bifunctional contrast agent, ACS Nano 10 (2016) 3783—3790.

[56] H. Xing, S. Zhang, W. Bu, X. Zheng, L. Wang, Q. Xiao, et al., Ultrasmall NaGdF4 nanodots for efficient MR angiography and atherosclerotic plaque imaging, Adv. Mater. 26 (2014) 3867—3872.

[57] A.K. Iyer, G. Khaled, J. Fang, H. Maeda, Exploiting the enhanced permeability and retention effect for tumor targeting, Drug Discov. Today 11 (2006) 812—818.

[58] F. Chen, S. Goel, R. Hernandez, S.A. Graves, S. Shi, R.J. Nickles, et al., Dynamic positron emission tomography imaging of renal clearable gold nanoparticles, Small 12 (2016) 2775—2782.

[59] F. Chen, H. Hong, Y. Zhang, H.F. Valdovinos, S. Shi, G.S. Kwon, et al., In vivo tumor targeting and image-guided drug delivery with antibody-conjugated, radiolabeled mesoporous silica nanoparticles, ACS Nano 7 (2013) 9027—9039.

[60] C.D. Walkey, J.B. Olsen, H. Guo, A. Emili, W.C. Chan, Nanoparticle size and surface chemistry determine serum protein adsorption and macrophage uptake, J. Am. Chem. Soc. 134 (2012) 2139—2147.

[61] C.D. Walkey, W.C. Chan, Understanding and controlling the interaction of nanomaterials with proteins in a physiological environment, Chem. Soc. Rev. 41 (2012) 2780—2799.